

Actions of highly eccentric orbits

Tom Wright¹ James Binney^{2*}

¹*Somerville College, Oxford OX1*

²*Rudolf Peierls Centre for Theoretical Physics, Clarendon Laboratory, Oxford, OX1 3PU, UK*

9 December 2025

ABSTRACT

The challenge presented by computing actions for eccentric orbits in axisymmetric potentials is discussed. In the limit of vanishing angular momentum about the potential's symmetry axis, there is a clean distinction between box and loop orbits. We show that this distinction persists into the regime of non-zero angular momentum. In the case of a Stäckel potential, there is a critical value $I_{3\text{crit}}(E)$ of the third integral I_3 below which I_3 does not contribute to the centrifugal barrier. An orbit is of box or loop type according as its value of I_3 is smaller or greater than $I_{3\text{crit}}$. We give algorithms for determining $I_{3\text{crit}}(E)$ and the critical action $J_{z\text{crit}}$ below which orbits in any given potential are boxes. It is hard to compute the actions and especially the frequencies of orbits that have $J_z \simeq J_{z\text{crit}}$ using the Stäckel Fudge. A modification of the Fudge that alleviates the problem is described.

Key words: Galaxy: kinematics and dynamics – galaxies: kinematics and dynamics – methods: numerical

1 INTRODUCTION

The Sun and most of its neighbours are on orbits that are not highly eccentric. By contrast, most of the stars that comprise the Galaxy's stellar halo are on highly eccentric orbits, and simulations of the clustering of dark matter suggest that most dark-matter particles are also on highly eccentric orbits. It follows that highly eccentric orbits will be important for any realistic Galaxy model.

Angle-action variables were invented to analyse the dynamics of the solar system, and our understanding of the structure and evolution of planetary systems is hugely dependent on insights obtained from angle-action coordinates. In light of this fact, it's natural to seek angle-action coordinates for galaxies.

Highly eccentric orbits are not especially difficult to compute by numerical integration of the equations of motion, but such integrations do not deliver values for an orbit's radial and vertical actions, J_r and J_z . Knowledge of orbits' values of these constants of motion is valuable because actions have many properties that other constants of motion, such as the orbits' initial conditions do not possess. Moreover, actions are the only constants of motion that can be embedded as the 'momenta' of a system of canonical coordinates, the conjugate variables being the 'angle' coordinates θ_i .

Galaxies are not precisely in equilibrium but they are

nearly in equilibrium, so their dynamics and evolution are naturally understood via perturbation theory. Action-angle coordinates are the bedrock on which Hamiltonian perturbation theory rests.

To be useful, angle-action coordinates must be computable. Classically they are derived from the solution $S(\mathbf{x}, \mathbf{J})$ of Hamilton-Jacobi equation – $S(\mathbf{x}, \mathbf{J})$ is the generating function of the canonical transformation from ordinary phase-space coordinates (\mathbf{x}, \mathbf{v}) to angle-action coordinates $(\boldsymbol{\theta}, \mathbf{J})$. Unfortunately, this nonlinear partial differential equation on real space can be solved only for very special potentials, and we know (from the occurrence of orbit trapping at resonances) that it is in principle impossible to solve it for the actual potentials of galaxies. Consequently, in the case of a real galaxy we must be content with systems of angle-action coordinates such that the actions are only approximately constant. Then we can solve for the time evolution of the actions by perturbation theory.

The PhD thesis of P.T. de Zeeuw (de Zeeuw 1985) was seminal because it established that galaxies have gravitational potentials that are in significant respects similar to the potentials that Stäckel investigated a century earlier, which give rise to separable Hamilton-Jacobi equations.

Currently three schemes for assigning suitable angle-action coordinates to phase-space points (\mathbf{x}, \mathbf{v}) are available: the 'Stäckel Fudge' (Binney 2012a) yields $(\boldsymbol{\theta}, \mathbf{J})$ given (\mathbf{x}, \mathbf{v}) ; Sanders & Binney (2014) give an algorithm for determining the actions of numerically integrated orbits; and torus mapping (Binney & McMillan 2016; Binney et al. 2025) yields

* E-mail: binney@physics.ox.ac.uk

(\mathbf{x}, \mathbf{v}) given $(\boldsymbol{\theta}, \mathbf{J})$. In this paper we focus on difficulties that arise when these techniques are applied to highly eccentric orbits.

Section 2 reviews the nature of orbits in axisymmetric potentials and explains how the sharp division of these orbits into two classes at $J_\phi = 0$ persists to non-zero J_ϕ . It explains the role that J_z plays in establishing a centrifugal barrier at small radii and explains how the action $J_{z\text{crit}}$ that divides the box and loop regimes can be computed. Section 3 explains how the Stäckel Fudge can perform poorly when $J_z \simeq J_{z\text{crit}}$ and J_z is contributing only marginally to the barrier. A workaround is proposed in Section 3.2. Section 4 sums up and explains why the algorithm given in Section 2.2 is important.

2 ORBITS IN A FLATTENED POTENTIAL

Orbits with $J_z = 0$ are confined to the equatorial plane. Each orbit occupies an annulus whose width increases with J_r/J_ϕ – circular orbits have $J_r = 0$. The value of J_z/J_ϕ indicates an orbit’s inclination i , which is zero when $J_z = 0$ and tends to 90 deg as $J_z/J_\phi \rightarrow \infty$. An orbit’s eccentricity is quantified by J_r/L , where $L = J_z + |J_\phi|$ is the extension to a non-spherical potential of the total angular momentum. Orbits with $J_r = 0$ are circular if $J_z = 0$, or ‘shell orbits’ when $J_z > 0$ – these are analogues of the inclined circular orbits of a spherical potential.

An instructive starting point for the study of eccentric orbits is the action-space plane $J_\phi = 0$. The orbits of this plane are confined in real space to a plane whose axes we call x and z . The z coordinate is the same as the galaxy’s vertical coordinate while x runs along a line within the equatorial plane. Within this plane, the gravitational potential is barred, x being the long axis and z being the short axis. Consequently, orbits with $J_\phi = 0$ divide into loop orbits and box orbits (e.g. Binney & Tremaine 2008, §3.3). The simplest box orbit comprises an oscillation along the x axis. A general box orbit is obtained by adding an oscillation parallel to the z axis. The actions J_x and J_z quantify the amplitudes of these two oscillations. When J_z exceeds a critical value, the x and z oscillations lock together to form a loop orbit, which occupies an elliptical annulus in real space. Now J_z quantifies the central semi-major axis of the annulus and J_r quantifies the annulus’s width: J_z has morphed into a generalised angular momentum and J_r has become a measure of eccentricity.

Fig. 1 is a typical (x, v_x) surface of section (SoS) for orbits with $J_\phi = 0$ – the figure is computed for a perfect ellipsoid (de Zeeuw 1985) of unit mass and scale-length a , and axis ratio $c/a = 0.6$, but the corresponding surface of section for many galactic potentials would be qualitatively the same. Each curve is a cross section through an orbital torus $\mathbf{J} = \text{constant}$. All tori have the same energy, so the value of J_r follows once J_z is specified. The larger orange curve is the torus $J_z = 0$ and J_z increases monotonically as we proceed inwards. The curves that lie between the orange curves are generated by box orbits, while those that lie inside the inner orange curve are generated by loop orbits. At the centre of the smallest curve lies the point generated by the shell orbit $J_r = 0$. Let $J_{z\text{crit}}$ be the value of J_z for the inner orange curve that separates boxes from loops.

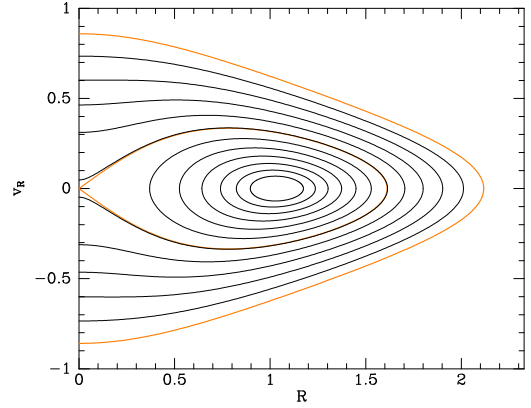


Figure 1. Surface of section at $E = \Phi(0)/2$ and $J_\phi = 0$ in the potential of a perfect oblate ellipsoid with scale lengths $a = 1$ and $c = 0.6$. At this energy the circular angular momentum is $L_{\text{circ}} = 0.663$.

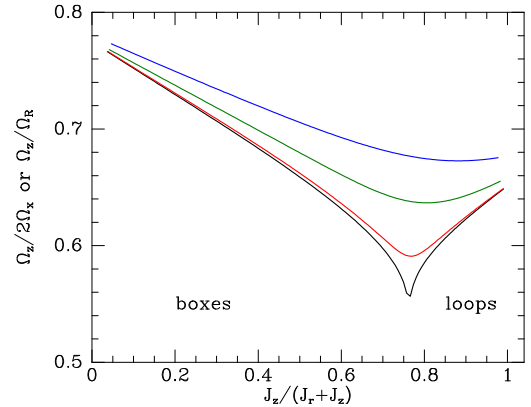


Figure 2. The ratio of vertical to horizontal frequencies as a function of circularity $J_z/(J_r + J_z)$ for the orbits with the energy of Fig. 1. The four curves are for $J_\phi = 0$ (black), $J_\phi = 0.02$ (red), $J_\phi = 0.1$ (green) and $J_\phi = 0.2$ (blue). We plot $\Omega_z/2\Omega_x$ for box orbits and Ω_z/Ω_R for loop orbits.

The black curve in Fig. 2 shows the variation with the circularity $c = J_z/(J_r + J_z)$ of the ratio of the vertical and horizontal frequencies at the energy of Fig. 1. The curve’s sharp minimum occurs at $J_z = J_{z\text{crit}}$. Box orbits lie to the left of this minimum, loop orbits lie to its right. In the regime of box orbits, the frequency Ω_z of vertical oscillations exceeds the long-axis frequency Ω_x . As J_z increases, the two frequencies converge. At the transition, the horizontal frequency switches from Ω_x to $\Omega_r \simeq 2\Omega_x$ and in the loop-orbit regime Ω_z/Ω_r rises with J_z .

Fig. 3 is the surface of section for the same potential and energy as Fig. 1 but $J_\phi = 0.02$ – for comparison, the circular angular momentum at the plot’s energy is $L_{\text{circ}} = 0.633$. Now the bounding orange curve $J_z = 0$ does not cross the v_R axis but plunges almost vertically very close to the axis, as do sections of four of the black curves within it. The smaller curves in Fig. 3 don’t have near-vertical left-hand sections. The red curve of Fig. 2 shows the corresponding variation of the frequency ratio, which differs from that when $J_\phi = 0$ mainly in the disappearance of the cusp at $J_z = J_{z\text{crit}}$. In particular, the red curve divides into falling and rising segments either side of $J_{z\text{crit}}$, so the distinction between box

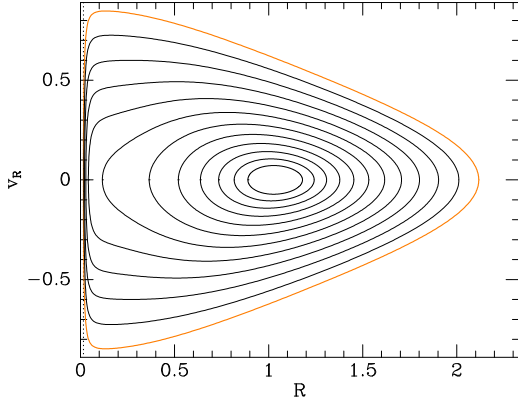


Figure 3. Surface of section at $J_\phi = 0.02$ for the orbits with the energy of Fig. 1.

and loop orbits has not been lost by introducing non-zero J_ϕ even though the appearance of the SoS has changed qualitatively between Figs. 1 and 3. The green and blue curves show the frequency ratios when $J_\phi = 0.1$ and 0.2 , respectively. The curve for $J_\phi = 0.1$ slopes upwards on the extreme right, while when $J_\phi = 0.2$ the upward-sloping section is on the point of vanishing.

Physically orbits with infinitesimal J_ϕ differ infinitesimally from orbits with vanishing J_ϕ notwithstanding the qualitative change in the SoS between Figs. 1 and 3: when $J_\phi = 0$ the orbit repeatedly cuts the z axis, while when $J_\phi = \epsilon$ it passes the axis at $y \simeq \epsilon/v_x$; when $J_\phi \neq 0$ the orbit is not confined to the xz plane but moves a bit further from his plane with each near-miss of the axis. Whereas with $J_\phi = 0$, the sign of v_R instantaneously changes at $x = 0$, with $J_\phi \neq 0$ the reversal of v_R occurs continuously over the small range in x at which $R = \sqrt{x^2 + y^2}$ is not dominated by x . Hence it is natural that the distinction between box and loop orbits, which is evident at $J_\phi = 0$, is also significant when J_ϕ is non-zero but small.

Fig. 4 shows analogues of Figs. 1 and 2 at a higher energy, $E = \Phi(0)/4$. The curves extend to larger J_z because more energy is available, but $J_{z,\text{crit}}$, which lies at the minimum of the black curve, has not increased so much, with the consequence that the right-hand segments of the curves, associated with loop orbits, have grown in importance relative to the left-hand segments, which are associated with box orbits. As J_ϕ increases, the minimum becomes less sharp but moves very little horizontally. The largest possible value of J_z decreases as J_ϕ increases because J_ϕ is being varied at constant energy and it ties up energy that cannot be invested in J_z . It follows that the value of J_z at the minimum is a decreasing function of J_ϕ .

Fig. 5 shows frequency ratios that involve Ω_ϕ as functions of circularity at several fixed values of J_ϕ . The full black curve, which is for J_ϕ equal to one percent of its circular value, shows that $\Omega_r = 2\Omega_\phi$ in the box-orbit regime on the left, while Ω_r falls more and more below $2\Omega_\phi$ in the loop-orbit regime on the right. The full red curve shows that Ω_z exceeds Ω_ϕ in the box-orbit regime but equals it in the loop-orbit regime. The broken curves generated by orbits with larger values of J_ϕ show that as J_ϕ is increased, the links between Ω_ϕ and Ω_r or Ω_z in the box-orbit or loop-

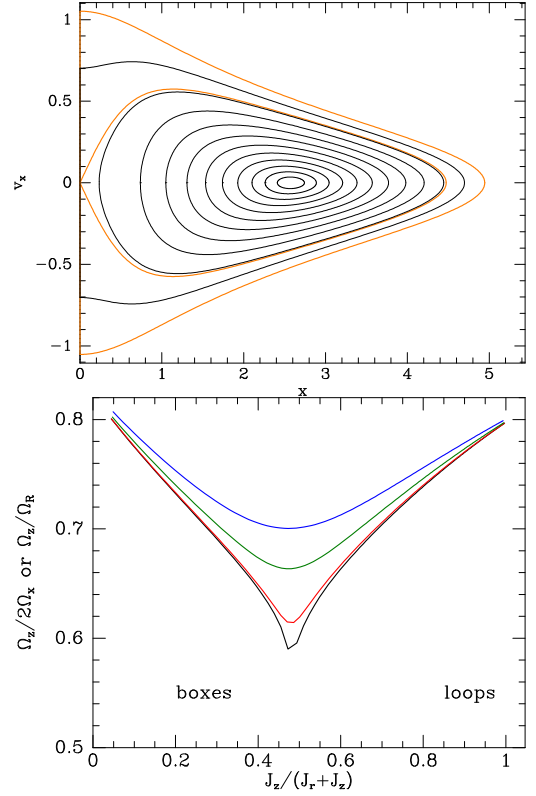


Figure 4. The analogues of Figs. 1 and 2 at a higher energy, namely $E = \Phi(0)/4$.

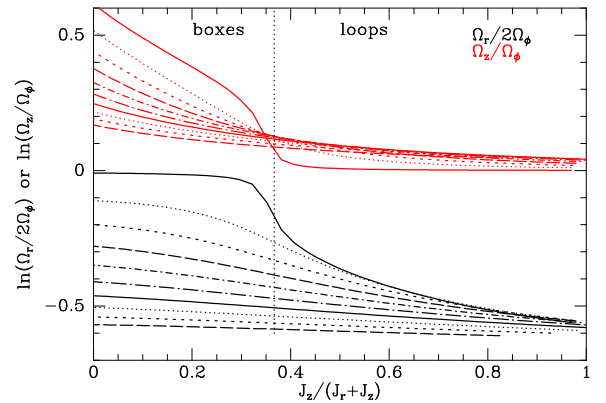


Figure 5. Frequency ratios for orbits of low J_ϕ in a flattened perfect ellipsoid. All orbits pass through $(R, z) = (3a, 0)$, where a is the scale radius of the ellipsoid. In the case of the top full curve in each panel the velocity there is $(v_R, v_z, v_\phi) = (V_m \sin \theta, V_m \cos \theta, 0.01V_c)$ where V_c is the circular speed at R and V_m yields the energy of the circular orbit at R . The n^{th} broken curves below the top curve on the left corresponds to $V_\phi = (0.01 + n/10)V_c$.

orbit regimes become weaker and the transition between the regimes becomes less sharp.

2.1 Centrifugal barriers

At the extreme left of Fig. 3 there is a dotted vertical line. This marks the pericentric radius of the planar orbit $J_z = 0$,

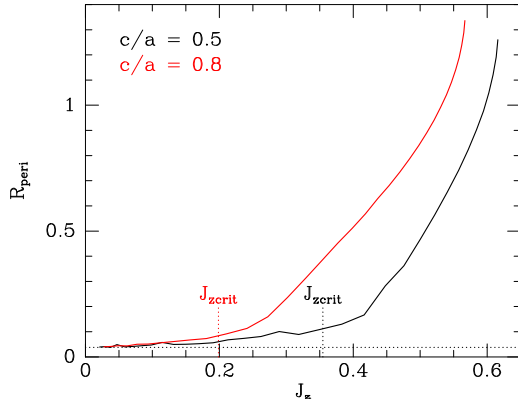


Figure 6. The full lines show the smallest value of R reached on numerically integrated orbits of energy $E = -0.3$ and $J_\phi = 0.05L_{\text{circ}}(R_{\text{shell}})$ in two NFW-like potentials with unit scale lengths: ones flattened to $c/a = 0.5$ (black) and 0.8 (red). The critical values of J_z in these potentials are marked by vertical dotted lines. The dotted horizontal line shows the smallest values of R reached on the planar orbit defined by the same values of J_r and J_ϕ but $J_z = 0$. Both potentials have out cut-off radii of 10 and unit `densityNorm`.

which is set by J_ϕ : it marks the ‘centrifugal barrier’ imposed by non-vanishing J_ϕ . Box orbits are kept away from the z axis by this barrier. Loop orbits do not approach this barrier because they are subject to a centrifugal barrier to which both J_z and J_ϕ contribute. The simplest way to grasp this phenomenon is to recall that the effective potential for motion in a spherical potential has a contribution $L^2/2r^2$ where $L \equiv J_z + |J_\phi|$ is the total angular momentum, so J_z helps set the barrier. When the potential is flattened, the contribution of J_z to the centrifugal barrier first becomes significant when J_z reaches the critical value $J_{z\text{crit}}$.

The full curves in Fig. 6 illustrates this phenomenon by plotting the pericentric radii R_{peri} of orbits with $J_\phi = 0.05L_{\text{circ}}$ in the potentials generated by bodies with the Navarro et al. (1997) (NFW) density profile that have been flattened to axis ratio $c/a = 0.5$ (black curve) or to $c/a = 0.8$ (red curve). As J_z decreases, the curves first plunge rapidly and then flatten off markedly when J_z is just a bit bigger than $J_{z\text{crit}}$. Thereafter they asymptote to the pericentric radius of the planar orbit $J_z = 0$ with the same value of J_ϕ , which is marked by the horizontal dotted black line.

2.2 Determination of $J_{z\text{crit}}$

The last section established that $J_{z\text{crit}}$ plays a significant role and it’s important to be able to determine it as a function of energy in realistic potentials. This is a non-trivial task because all available algorithms for determining actions (the Stäckel Fudge, torus mapping and extraction of $S(\mathbf{x}, \mathbf{J})$ from a numerically integrated orbit) fail when confronted with orbits near the box-loop transition. Here we describe the algorithm for the determination of $J_{z\text{crit}}(E)$ that we have coded into the AGAMAB (Binney et al. 2025) branch of the AGAMA software library (Vasiliev 2019a).

If we drop a star from a point $z = Z$ on the z axis, the star will remain on the axis and return after completing the (unstable) ‘short-axis orbit’ of energy $E = \Phi(0, Z, 0)$. A box orbit with energy E and $J_z \simeq J_{z\text{crit}}(E)$ can be generated

by dropping a star from infinitesimally off the z axis where $\Phi = E$. The star falls to the centre, comes to rest at negative z before returning and coming to rest extremely close to its point of departure. From the orbit’s time sequence we can evaluate¹

$$J_{\text{fast}} = \frac{1}{2\pi} \oint dz p_z. \quad (1)$$

We now show that

$$J_{\text{fast}} = J_z + 2J_r. \quad (2)$$

We consider the case that the star is moving in a Stäckel potential. Such a potential is associated with a system (u, v) of confocal ellipsoidal coordinates such that

$$\begin{aligned} R &= \Delta \sinh u \sin v \\ z &= \Delta \cosh u \cos v, \end{aligned} \quad (3)$$

where Δ is the z coordinate of one focus. The system’s ellipses in the xz plane are labelled by $u \geq 0$ and its hyperbolae are labelled by v . We exploit that

$$p_R dR + p_z dz = p_u du + p_v dv \quad (4)$$

because both coordinate systems are canonical.

As the star falls from its point of release at $z = Z \leftrightarrow u = U$, to the focus of the potential’s coordinate system at $z = \Delta \leftrightarrow u = 0$, its value of v is constant at $v = \pi/2$. Hence,

$$\int_Z^\Delta dz p_z = \int_U^0 du p_u. \quad (5)$$

As the star travels from $z = \Delta$ to $z = -\Delta$, v changes from $\pi/2$ to $-\pi/2$ while u remains fixed at zero. So

$$\int_\Delta^{-\Delta} dz p_z = \int_{\pi/2}^{-\pi/2} dv p_v. \quad (6)$$

As the star moves from $z = -\Delta$ to $z = -Z$, v is constant at $-\pi/2$ while u returns from zero to U , so

$$\int_{-\Delta}^{-Z} dz p_z = \int_0^U du p_u, \quad (7)$$

where $p_u > 0$ whereas in equation (5) $p_u < 0$. These three stages are then executed in reverse order, with reversed limits of integration and changed signs on the momenta. Adding all the integrals, we find

$$J_{\text{fast}} = \frac{1}{\pi} \oint du p_u + \frac{1}{2\pi} \oint dv p_v. \quad (8)$$

This equation establishes equation (2) in the case of a Stäckel potential because then $2\pi J_r = \oint du p_u$ and $2\pi J_z = \oint dv p_v$.

Equation (2) generalises to any potential because J_{fast} is defined by a closed path around an orbital torus so it has to be an integer linear combination of the actions. The integer multipliers are constant as we deform the potential into a Stäckel potential.

The critical orbit’s value of J_r can be obtained from the area inside the orbit’s trace in a SoS such as Fig. 1. Substituting this value into equation (2), we obtain $J_{z\text{crit}}$.

As $E \rightarrow 0$ (marginally bound orbits), it becomes hard to

¹ J_{fast} would be the conserved ‘fast’ action in a perturbative treatment of the box-loop transition.

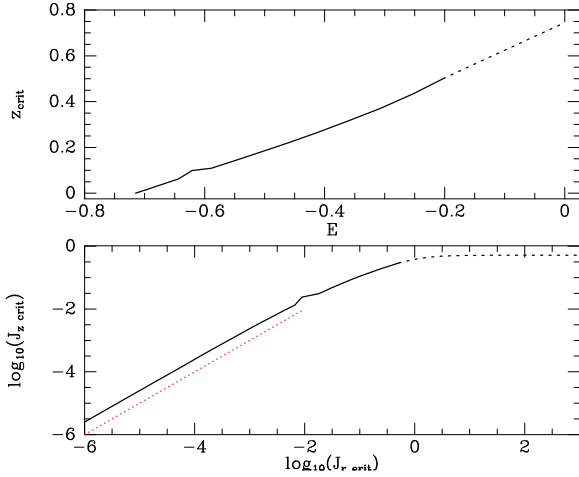


Figure 7. Upper panel: z_{crit} versus E for the NFW-like potential of Fig. 6 for axis ratio $c/a = 0.8$. The full portion was obtained from equation (9) using values of $J_{z,\text{crit}}$ that follow from equation (2) with J_r estimated from a SoS. The dashed portion is the adopted linear extrapolation of the full portion. Lower panel: the resulting graph of $J_{z,\text{crit}}$ as a function of $J_{r,\text{crit}}$. The red dotted line shows $y = x$.

accumulate sufficient consequents for accurate evaluation of the area so we employ the following extrapolation procedure. We define $z_{\text{crit}}(E)$ by

$$J_{z,\text{crit}} = \frac{2}{\pi} \int_0^{z_{\text{crit}}} dz p_z, \quad (9)$$

where $p_z(z|E)$ is the momentum along the short-axis orbit. The argument given above shows that in the case of a Stäckel potential $z_{\text{crit}} = \Delta$ when $Z < \Delta$, where Z is, as before, such that $E = \Phi(0, Z, 0)$. In the general case, we can solve equation (9) for $z_{\text{crit}}(E)$ on a grid of values of E low enough for $J_{z,\text{crit}}$ to be obtained as described above. At the largest of these E values, z_{crit} tends to a linear function of E – illustrated by the upper panel of Fig. 7. By extrapolating this function, we can predict z_{crit} for higher E , and then obtain the corresponding values of $J_{z,\text{crit}}$ from equation (9) – the lower panel of Fig. 7 shows the resulting function $J_{z,\text{crit}}(J_{r,\text{crit}})$ for one of the NFW-like potentials of Fig. 6. At low energies $J_{z,\text{crit}} \propto J_{r,\text{crit}}$ implying that a fixed fraction of orbits are loops. At high energies, by contrast, $J_{z,\text{crit}}$ asymptotes to a constant, implying that an ever increasing fraction of orbits are loops.

2.3 Numerical implementation

When a potential is ‘created’ in the software package AGAMAB, box/loop transition orbits are computed over essentially all energies so that subsequently $J_{z,\text{crit}}$ can be recovered as functions of J_{fast} from the potential’s method `getJzcrit`. Also stored at this stage are the values $I_{3,\text{crit}}(E)$ of the transition orbits. They are evaluated at $(\mathbf{x}, \mathbf{v}) = (R_{\text{shell}}, 0, 0, v_R, v_z, 0)$, where v_R is obtained from the surface of section from which J_r is computed and v_z then follows from the value of E – it matters where I_3 is evaluated because I_3 isn’t an exact constant of motion in a general potential. $I_{3,\text{crit}}(E)$ can subsequently be recovered from the potential’s method `getI3crit`.

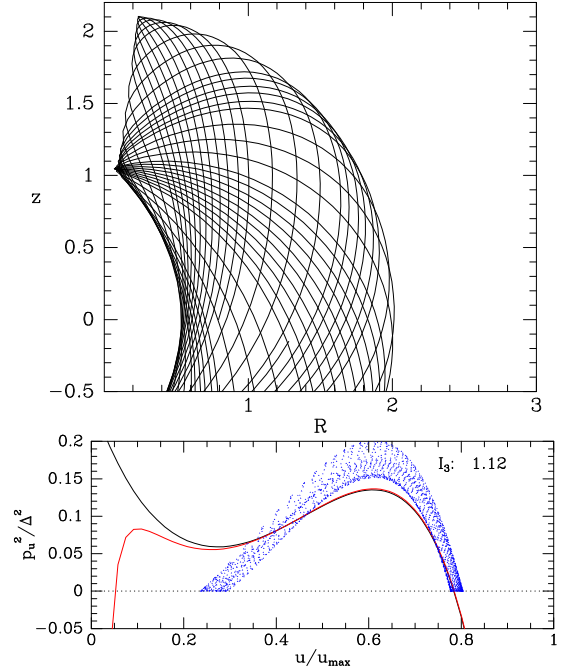


Figure 8. An orbit with $J_\phi = 0.05 L_{\text{circ}}(R_{\text{shell}})$ in the NFW-like potential used to make the black curve in Fig. 6. The upper panel shows the orbit in the meridional plane. The blue points in the lower panel show the points (u, p_u^2) through which the orbit passes when the focal distance of the (u, v) coordinate system is fitted to the shell orbit at the given values of E and J_ϕ . The red curve shows the values of $p_u^2(u)$ predicted by the full effective potential (eqn. 10), while the black curve shows the value of p_u^2 predicted by the effective potential obtained by setting $J_\phi = 0$.

3 APPLICATION TO THE STÄCKEL FUDGE

The Stäckel Fudge has been widely used to compute actions in realistic galactic potentials (e.g. Binney 2012b; Sanders & Binney 2013; Bovy & Rix 2013; Bovy 2014; Posti et al. 2015; Binney & Wong 2017; Binney & Schönrich 2018; Pascale et al. 2018, 2019; Vasiliev 2019b; Bland-Hawthorn et al. 2019; Bland-Hawthorn & Tepper-Garcia 2021). It involves choosing a length Δ that defines a coordinate system (u, v) via equations (3), and then applying to the given potential formulae that are strictly only valid for a Stäckel potential. In the widely used implementation of the Fudge contained in the AGAMA code library (Vasiliev 2019a) Δ is set to the value Δ_{shell} that fits the shell orbit $J_r = 0$ that has the same energy and angular momentum J_ϕ as the orbit under study.

The merit of a value of Δ is conveniently assessed by computing an orbit in the given potential and then plotting the resulting data points $(\mathbf{x}_i, \mathbf{v}_i)$ in the (u, p_u) plane: ideally Δ is chosen such that every point (u, p_u) lies on a curve rather than filling out a zone of non-zero area.

3.1 A problem with the Fudge

The upper panel of Fig. 8 shows the trace in the meridional plane of an orbit in the potential associated with the black curve in Fig. 6. The blue points in the lower panel show the locations (u, p_u) through which the orbit passes in the coordinate system defined by the focal distance Δ_{shell} that fits the shell orbit of the given (E, J_ϕ) . The red curve shows

the values $p_u^2(u)$ upon which the Stäckel Fudge relies. This functional form arises from a definition of the third integral I_3 of a Stäckel potential:²

$$I_3 = E \cosh^2 u - \frac{1}{2\Delta^2} \left(p_u^2 + \frac{J_\phi^2}{\sinh^2 u} \right) - U(u). \quad (10)$$

where $U(u)$ is the function that defines a Stäckel potential through

$$\Phi(u, v) = \frac{U(u) - V(v)}{\sinh^2 u + \sin^2 v}. \quad (11)$$

The central idea of the Stäckel Fudge is that for potentials $\Phi(u, v)$ similar to those of axisymmetric galaxies, a value u_0 can be chosen such that

$$\delta U \equiv (\sinh^2 u + \sin^2 v) \Phi(u, v) - (\sinh^2 u_0 + \sin^2 v) \Phi(u_0, v) \quad (12)$$

has only weak dependence of v , so $\delta U + U(u_0)$ can be used in equation (10) in place of $U(u)$. Equation (10) yields $p_u^2(u)$ once the constant of motion $I_{3u} \equiv I_3 + U(u_0)$ has been determined from the initial conditions. Similarly, p_v^2 can be determined from

$$I_{3v} = -E \sin^2 v + \frac{1}{2\Delta^2} \left(p_v^2 + \frac{J_\phi^2}{\sin^2 v} \right) - \delta V(v), \quad (13)$$

where $I_{3v} \equiv I_3 - V(\pi/2)$ can be determined from the initial conditions and we neglect the u dependence of

$$\delta V \equiv \cosh^2 u \Phi(u, \pi/2) - (\sinh^2 u + \sin^2 v) \Phi(u, v). \quad (14)$$

The optimum value of u_0 is such that

$$R_{\text{shell}} = \Delta \sinh u_0, \quad (15)$$

where R_{shell} is the radius at which the shell orbit crosses the equatorial plane. Hence u_0 and I_{3u} follow once Δ has been chosen.

In Fig. 8 we plot p_u^2/Δ^2 because p_u is equal to Δ times a linear combination of p_R and p_z . Consequently, when we change Δ , p_u^2/Δ^2 does not change much at given u . For this reason, equations (10) and (13) show that the values of I_{3u} and I_{3v} recovered from initial conditions are weakly dependent on Δ .

The problem that Fig. 8 illustrates is that the blue points reach the dotted line $p_u^2 = 0$ significantly to the right of the red curve. That is, the effective potential defined by the Fudge predicts that the orbit penetrates to significantly smaller radii than it actually does because I_3 is not providing a centrifugal barrier where it should.

The definition of I_3 is such that at a given energy I_3 increases from zero on an orbit that lies within the equatorial plane, to a maximum value

$$I_{3\text{max}} = \frac{R_{\text{shell}}^2 + \Delta^2}{2\Delta^2} v_z^2, \quad (16)$$

on the shell orbit $J_r = 0$, which moves through the plane at speed v_z . Hence, when $R_{\text{shell}} \gg \Delta$, on a shell orbit $I_3 \simeq \frac{1}{2}(J_z/\Delta)^2$ generates a centrifugal exclusion zone around the centre barrier by forcing p_u to zero at a non-zero value of u .

² Eqn. (10) is E plus the definition of I_3 used by Binney (2012a). The definition used in both AGAMA and AGAMAb differs by a factor Δ^2 , so I_3 in the code has the dimensions of action squared rather than energy. Discussion of changes in Δ is simpler without this factor of Δ .

The black curve in the lower panel of Fig. 8 plots the value of p_u^2 that one obtains from equation (10) with $J_\phi = 0$. This curve, which deviates from the red curve only at small u , does *not* dip below the u axis at small u , so it fails to exclude the star from the centre, implying that this is a box orbit; the box/loop transition of orbits with $J_\phi = 0$ occurs at the value of I_3 that causes the black curve's minimum to lie on $p_u^2 = 0$. In the case of the loop orbit plotted in Fig. 8, the minimum should lie at $p_u^2 < 0$, because J_z is contributing to the orbit's exclusion from the origin.

3.2 The work-around

Diminishing the value of Δ pushes the red and black curves in Fig. 8 down, and for a suitable value of Δ , p_u^2 can be made to turn negative where the blue points terminate, and this is the best value of Δ . Hence as we move from the shell orbit to more eccentric loop orbits, we should adjust Δ such that the black curve continues to reach the u axis where the blue points terminate. The smallest value of u at which the black curve can reach $p_u^2 = 0$ is the location of the curve's local minimum. The boxes start when this minimum first occurs at $p_u^2 > 0$ so the blue points are free to move to the centrifugal barrier set by J_ϕ . For the transition to be modelled as smooth, as it really is when $|J_\phi| > 0$, the location u_{min} of the minimum as it lifts off the u axis should be close to the location of the centrifugal barrier set by J_ϕ (where the red curves crosses the u axis in Fig. 8).

In summary, the black curve in Fig. 8 quantifies the dynamics in the absence of J_ϕ . It has a local minimum and if this occurs at $p_u^2 > 0$, the star could reach $u = 0$ in the absence of J_ϕ ; conversely, when the minimum occurs at $p_u^2 \leq 0$, the star is excluded from $u = 0$ even when $J_\phi = 0$. That is, a centrifugal barrier associated with J_z exists if and only if the minimum occurs at $p_u^2 \leq 0$. Since exclusion from $u = 0$ is the hallmark of loop orbits, for loop orbits we must ensure that the minimum occurs at $p_u^2 \leq 0$ while for box orbits the minimum should occur at $p_u^2 > 0$. At the box/loop transition, the minimum falls on the u axis.

From the equations $p_u^2 = 0$ and $dp_u^2/du = 0$ we can solve for the largest focal distance, Δ_{excl} , for which J_z acting alone excludes the star from $u = 0$. During the survey of box/loop transition orbits that is performed when AGAMAb creates a potential, values of $\Delta_{\text{crit}}(E) = \Delta_{\text{excl}}(E, I_{3\text{crit}})$ are stored so they can be subsequently recovered by calling the potential's method `getFDcrit`. The code also stores the value u_{min} of u at which $p_u^2 = 0$ – they can be recovered from the potential's method `getUmin`.

When action-angle variables are to be computed for a highly eccentric orbit, the orbit's value of I_3 is compared with $I_{3\text{crit}}$. If I_3 is smaller than $I_{3\text{crit}}$, the orbit must be a box and I_3 does not generate a centrifugal barrier. Hence the focal distance must exceed $\Delta_{\text{excl}}(E, I_3)$ – the code uses the focal distance Δ_{shell} obtained from the corresponding shell orbit. If I_3 is equal to $I_{3\text{crit}}$, we are dealing with a transition orbit and we should use Δ_{crit} so the potential barrier generated by J_z is on the cusp of disappearing. When $I_3 > I_{3\text{crit}}$, the focal distance must be such that I_3 creates a centrifugal barrier, so we need $\Delta < \Delta_{\text{excl}}(E, I_3)$. As I_3

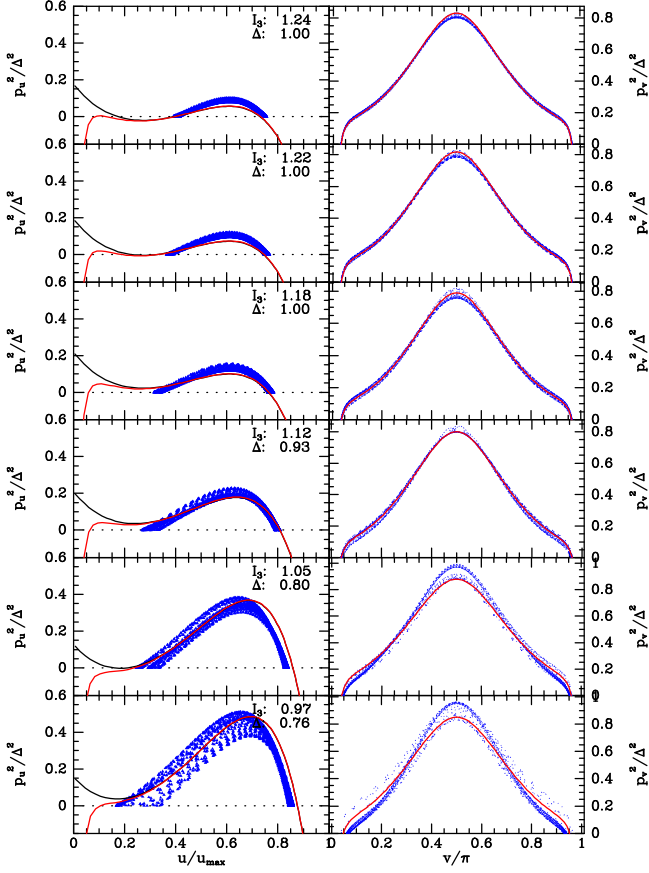


Figure 9. Six orbits plotted in the (u, p_u^2) and (v, p_v^2) planes when Δ is given by equation (17). The numbers at top right of the left column are $I_3/I_{3\text{crit}}$ and $\Delta/\Delta_{\text{shell}}$. All orbits have J_ϕ equal to 5 per cent of the circular angular momentum at R_{shell} .

tends to its maximum value, $I_{3\text{max}}$ (eqn. 16) Δ must tend to Δ_{shell} . The implemented variation of Δ with I_3 is

$$\Delta \equiv \begin{cases} \Delta_{\text{shell}} & I_3 \leq I_{\text{bot}} \\ \bar{\Delta} + \hat{\Delta} \cos \psi & I_{\text{bot}} < I_3 < I_{\text{top}} \\ \Delta_{\text{shell}} & I_3 \geq I_{\text{top}} \end{cases}, \quad (17)$$

where

$$\begin{aligned} I_{\text{bot}} &= I_{3\text{crit}} - 0.75(I_{3\text{max}} - I_{3\text{crit}}) \\ I_{\text{top}} &= I_{3\text{crit}} + 0.75(I_{3\text{max}} - I_{3\text{crit}}) \\ \psi &= 2\pi \frac{I_3 - I_{\text{bot}}}{I_{\text{top}} - I_{\text{bot}}} \\ \bar{\Delta} &\equiv \Delta_{\text{shell}} - \hat{\Delta} \quad \hat{\Delta} = \frac{\Delta_{\text{shell}} - \Delta_{\text{crit}}}{1 + \exp[4J_\phi^2/(\Delta^2 I_{3\text{max}})]}. \end{aligned} \quad (18)$$

With this rule, Δ changes from Δ_{shell} for $I_3 < I_{\text{bot}}$ to $\Delta_{\text{shell}} - 2\hat{\Delta}$ when $I_3 = I_{\text{crit}}$ and then grows, reaching Δ_{shell} at $I_3 = I_{\text{top}}$. When $J_\phi^2 \ll I_{3\text{max}}$, $\Delta_{\text{shell}} - 2\hat{\Delta} \simeq \Delta_{\text{excl}}$ but as $J_\phi^2/I_{3\text{max}}$ grows, $\hat{\Delta}$ diminishes and the classical Fudge is restored. Fig. 11 shows the values of Δ that produced Figs. 9 and 10.

Figs. 9 and 10 show the (u, p_u) and (v, p_v) planes for twelve orbits of increasing eccentricity when Δ is given by equation (17). As in Fig. 8, red and black curves in the left-hand panels show the values of p_u^2 given by the Stäckel formula. They delineate the blue points from the orbit in-

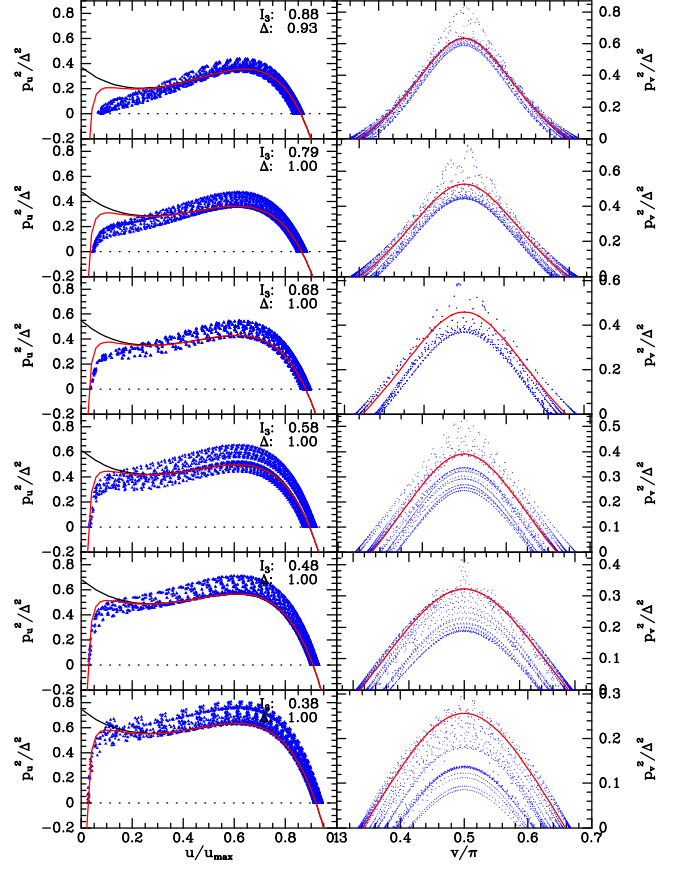


Figure 10. As Fig. 9 but for more eccentric orbits.

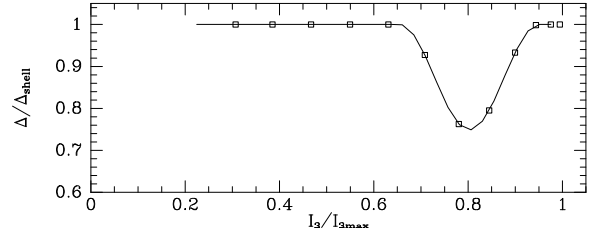


Figure 11. The variation of Δ with I_3 used to produce Figs. 9 and 10. The squares correspond to the orbits in those figures.

tegration reasonably well, especially when $I_3 > I_{3\text{crit}}$. Two significant shortcomings remain:

- In the third and fourth panels from the top of Fig. 9 the black curve doesn't quite reach $p_u^2 = 0$ even though $I_3 > I_{3\text{crit}}$. The code deals with this problem by taking $p_u^2 = 0$ for $u < u_{\text{min}}$, the location of the black curve minimum for $I_3 = I_{3\text{crit}}$.
- For the more eccentric orbits the blue points are not nicely marshalled onto a curve. This failure potentially compromises the returned values of J_z and Ω_z .

The black points in Fig. 12 show values of J_r returned by the Fudge along the orbits plotted in Figs. 9 and 10 when using Δ_{shell} (upper panel) or the values of Δ from equation (17). The magenta points show the corresponding values of J_z . The vertical extension of each group of points is a measure of the inaccuracy of the Fudge. Using variable Δ

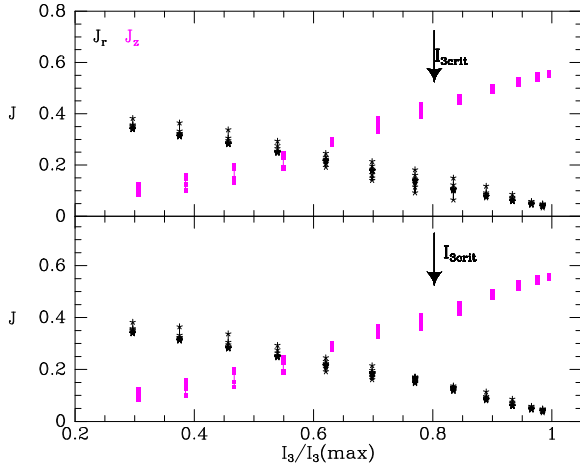


Figure 12. Actions along the sequence of orbits plotted in Figs. 9 and 10 as computed using Δ_{shell} (upper panel) and (lower panel) using variable Δ to eliminate the region of u where $p_u^2 < 0$. At each value of I_3 the actions are computed at 20 points along the numerically integrated orbit. For clarity the black points for J_r are displaced slightly in I_3 .

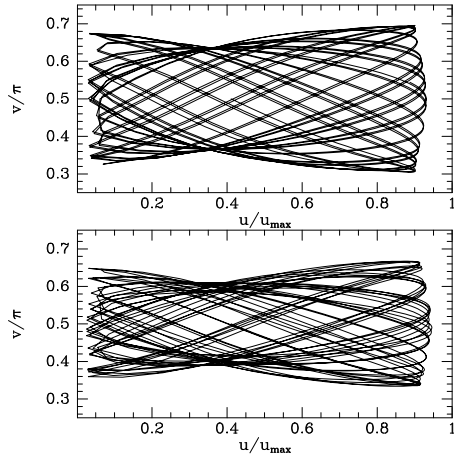


Figure 13. The traces in the (u, v) plane of the orbits giving rise to the lowest two panels in the column on the extreme right of Fig. 10. The nearly rectangular trace in the upper panel here is associated with a single arc in the (v, p_v^2) plane.

has little impact on the spread in J_z but it does significantly diminish the spread in J_r , especially when $I_3 \simeq I_{3\text{crit}}$.

Fig. 13 gives insight into why the blue points in the bottom right panel of Fig. 10 are grouped into two distinct arcs. It shows the (u, v) traces of that orbit (lower panel) and the trace of the orbit above it in Fig. 10, which produces a single (wide) arc in the (v, p_v^2) plane. In the lower panel of Fig. 13, the orbit has three distinct types of turning point in v . Two of these occur at the left and right corners of the roughly rectangular trace of the orbit. These turning points are associated with the feet of the larger arc in the bottom right panel of Fig. 10. The third type of turning point occurs at $u \simeq 0.35u_{\text{max}}$, $v \simeq 0.61\pi$ and is associated with the feet of the smaller arc in Fig. 10. The turning points of the orbit plotted in the upper panel of Fig. 13 are all of the first or second type, so the orbit generates a single arc in the (v, p_v^2) plane.

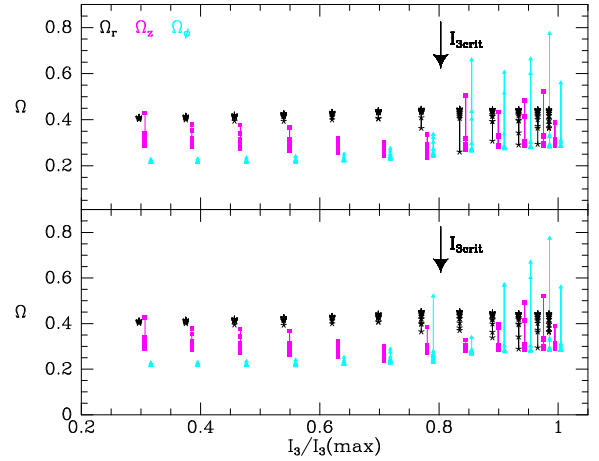


Figure 14. The same as Fig. 12 but showing values of the orbital frequencies Ω_r (black), Ω_z (magenta) and Ω_ϕ (cyan).

Near the middle of the upper edges of the traces in both panels there are regions in which the star transits along three lines rather than two. The existence of these regions implies that the orbit's third integral cannot be expressed as a quadratic in p_u and p_v as the Fudge requires. Fortunately the lines fall into two groups of nearly parallel lines so the Fudge can provide good approximations to the true velocities.

3.3 Frequencies

Orbital frequencies sometimes play a significant role in galactic dynamics, so we consider improvements in how AGAMAb computes them.

The Fudge computes frequencies by inverting the matrix $\partial J_i / \partial I_j$, where $\mathbf{I} = (E, I_3, J_\phi)$.³ When the integral for J_i is differentiated, p_i migrates to the denominator of the integrand. For example

$$\frac{\partial J_r}{\partial I_3} = -\frac{1}{\pi} \int_{u_{\min}}^{u_{\max}} \frac{du}{p_u}. \quad (19)$$

With the setup illustrated by Fig. 8, the adopted value of u_{\min} is too small because it is where the red curve passes through zero rather than the endpoint of the blue points, and p_u may be predicted to be very small in the spurious interval of integration. Hence the contribution of the spurious interval to $\partial J_r / \partial I_3$ can then be much greater than its contribution to $J_r \propto \oint du p_u$. It follows that the Fudge is liable to compute frequencies markedly less accurately than it computes actions.

Fig. 14 shows values returned for the frequencies of the orbits plotted in Figs. 9 and 10 when Δ is set to Δ_{shell} (upper panel) and when it is varied according to equation (17). As in Fig. 12, the vertical spread in each group of points reflects the Fudge's inaccuracy. With fixed Δ serious errors are apparent for $I_3 > I_{3\text{crit}}$. Varying Δ modestly reduces the error in Ω_r and Ω_z , especially near $I_{3\text{crit}}$ but does not provide a satisfactory resolution of the problem. The errors in Ω_ϕ remain unacceptably large.

³ The matrix $\partial J_i / \partial I_j$ is also involved in the computation of the angle variables $\theta_i(\mathbf{x}, \mathbf{v})$.

4 CONCLUSIONS

Even at non-zero J_ϕ it is useful to divide orbits in an axisymmetric potential into box and loop orbits. J_z contributes to the centrifugal barrier experienced by orbits only in the case of loop orbits. A procedure was described for computing the critical action $J_{z\text{crit}}$ below which orbits are boxes. Knowledge of $J_{z\text{crit}}$ proves to be important when constructing the tori of eccentric orbits (Binney et al. 2025) and when evaluating the distribution function of a spheroidal component (Binney 2026).

Particular care in the choice of the focal distance Δ is required when applying the Stäckel Fudge to orbits that have $J_z \simeq J_{z\text{crit}}$. The optimum value of Δ is the one that correctly predicts the smallest value of the ellipsoidal variable u to which the orbit penetrates. In an interval around $J_{z\text{crit}}$, this value proves smaller than the value Δ_{shell} that fits the shell orbit. The Stäckel Fudge action finder provided by AGAMAb reduces Δ in the vicinity of $J_{z\text{crit}}$, and as a consequence significantly reduces the scatter in the values of J_r computed along eccentric orbits. The computational cost of this upgrade is negligible.

Values of orbital frequencies are particularly vulnerable to sub-optimal choices of Δ . Unfortunately, the change that reduces the scatter in J_r has less impact on the scatter in frequencies.

Understanding that orbits in the meridional plane are of two distinct types proves crucial (a) for torus mapping, and (b) for structuring distribution functions $f(\mathbf{J})$ for stellar systems with anisotropic velocity distributions. Binney et al. (2025) extend torus mapping to almost radial orbits in flattened potentials by using harmonic-oscillator or isochrone toy maps according as J_z is smaller or larger than $J_{z\text{crit}}$. Possession of a convenient way of computing $J_{z\text{crit}}(J_{\text{fast}})$ enabled Binney (2026) to construct the first action-based DFs for anisotropic, flattened systems that yield physical velocity distributions in the neighbourhood of $v_\phi = 0$. Consequently, we expect the algorithm for computing $J_{z\text{crit}}(J_{\text{fast}})$ given in Section 2.2 and embedded in AGAMAb to play a significant role as angle-action variables are used to interpret data for galaxies of all types.

ACKNOWLEDGEMENTS

It's a pleasure to thank Eugene Vasiliev for extensive assistance in understanding why AGAMAb's Fudge was performing badly. This research was supported by the Leverhulme Trust under grant LIP-2020-014 and in part by grant NSF PHY-2309135 to the Kavli Institute for Theoretical Physics (KITP).

DATA AVAILABILITY

The computations were performed by C++ code linked to the AGAMAb library (Binney et al. 2025), which can be downloaded from <https://github.com/binneyox/AGAMAb>.

REFERENCES

Binney J., 2012a, MNRAS, 426, 1324

- Binney J., 2012b, MNRAS, 426, 1328
 Binney J., 2026, MNRAS, xx, 1898
 Binney J., McMillan P. J., 2016, MNRAS, 456, 1982
 Binney J., Schönrich R., 2018, MNRAS, 481, 1501
 Binney J., Tremaine S., 2008, Galactic Dynamics: Second Edition. Princeton University Press
 Binney J., Vasiliev E., Wright T., 2025, MNRAS, xxx, xxx
 Binney J., Wong L. K., 2017, MNRAS, 467, 2446
 Bland-Hawthorn J. et al., 2019, MNRAS, 486, 1167
 Bland-Hawthorn J., Tepper-Garcia T., 2021, MNRAS, 504, 3168
 Bovy J., 2014, ApJ, 795, 95
 Bovy J., Rix H.-W., 2013, ApJ, 779, 115
 de Zeeuw T., 1985, MNRAS, 216, 273
 Navarro J. F., Frenk C. S., White S. D. M., 1997, ApJ, 490, 493
 Pascale R., Binney J., Nipoti C., Posti L., 2019, MNRAS, 488, 2423
 Pascale R., Posti L., Nipoti C., Binney J., 2018, MNRAS, 480, 927
 Posti L., Binney J., Nipoti C., Ciotti L., 2015, MNRAS, 447, 3060
 Sanders J. L., Binney J., 2013, MNRAS, 433, 1826
 Sanders J. L., Binney J., 2014, MNRAS, 441, 3284
 Vasiliev E., 2019a, MNRAS, 482, 1525
 Vasiliev E., 2019b, MNRAS, 484, 2832